frontiers | Frontiers in Physics

TYPE Original Research
PUBLISHED 26 February 2024
DOI 10.3389/fphy.2024.1360083

Check for updates

OPEN ACCESS

EDITED BY
Florian Wiesinger,
GE Global Research, Germany

REVIEWED BY
Manoj Kumar Sarma,
University of Texas Southwestern Medical Center, United States
Jose Fernando de Arcos Rodriguez,
GE Healthcare, United Kingdom

*CORRESPONDENCE
Hanna Frantz,
hanna.frantz@uni-ulm.de

RECEIVED 22 December 2023
ACCEPTED 05 February 2024
PUBLISHED 26 February 2024

CITATION
Frantz H, Speidel T and Rasche V (2024), Single-petal rosette trajectory for 2D functional lung imaging.
Front. Phys. 12:1360083.
doi: 10.3389/fphy.2024.1360083

COPYRIGHT
© 2024 Frantz, Speidel and Rasche. This is an open-access article distributed under the terms of the Creative Commons Attribution License (CC BY). The use, distribution or reproduction in other forums is permitted, provided the original author(s) and the copyright owner(s) are credited and that the original publication in this journal is cited, in accordance with accepted academic practice. No use, distribution or reproduction is permitted which does not comply with these terms.

Single-petal rosette trajectory for 2D functional lung imaging

Hanna Frantz*, Tobias Speidel and Volker Rasche

Department of Internal Medicine II, University Ulm Medical Center, Ulm, Germany

Purpose: The purpose of this study was to investigate the use of a 2D rosette trajectory for breath-hold and free-breathing real-time imaging of the lungs.

Methods: Eight healthy volunteers underwent breath-hold magnetic resonance imaging (MRI) using two different parametrizations of the proposed single-petal rosette (SPR) trajectory, as well as radial ultra-short echo time (UTE) acquisition combined with the tiny golden-angle acquisition scheme. The additional free-breathing acquisitions of all trajectories were performed. The proposed technique was compared with the conventional radial UTE technique regarding image sharpness, signal-to-noise ratio (SNR), regional fractional ventilation (FV) for breath-hold and retrospective image-based self-gating, and real-time imaging capabilities.

Results: Image sharpness significantly increased for gated SPR images compared to radial UTE for the end-expiratory stage; no significant difference was found for the self-gated end-inspiratory stage and the breath-hold acquisitions. The SPR trajectory performs significantly better than radial UTE concerning the SNR for breath-hold imaging, whereas no significant difference was found for self-gated images. Fractional ventilation values were comparable between SPR and radial UTE. The SPR real-time data showed a marked reduction in the aliasing artifacts with no apparent streaks.

Conclusion: The second half of the petal of the SPR trajectory accomplishes rephasing while acquiring non-redundant k-space data, thus leading to a more efficient sampling of the k-space than that with the radial UTE sampling scheme, with a minimal increase in TR. This leads to the need of less read-outs to achieve the same SNR values and, thus, a reduction in scan time. For real-time application, the SPR approach resulted in a marked reduction of aliasing artifacts when compared to UTE.

KEYWORDS

lung magnetic resonance imaging, ultra-short echo time imaging, breath-hold, retrospective self-gating, image-based self-gating, functional imaging

1 Introduction

Over recent years, lung magnetic resonance imaging (MRI) has proven to be an attractive imaging modality for non-invasive evaluation of pulmonary function and structure. As the clinical demand for comprehensive lung assessment continues to increase, there is a growing interest in the development of innovative and reliable imaging techniques to address the challenges posed by lung MRI, including lung motion and low signal intensity in the lung parenchyma. In this context, MRI may especially be attractive for regional quantification of lung function, including fractional ventilation [1] (FV) and perfusion [2], which likely provides valuable insights into pulmonary physiology.

Fast data acquisition strategies play a pivotal role in overcoming the challenges associated with lung imaging. Traditionally, lung MRI has been hindered by long acquisition times, leading to motion artifacts and limited temporal resolution. To mitigate these limitations, novel imaging approaches, including parallel imaging [3, 4] and compressed sensing [5, 6], have been developed, alongside with radial (center-out) k-space sampling schemes, such as radial ultra-short echo time (UTE) [7] and zero echo time (ZTE) [8], by making use of their sub-Nyquist imaging capabilities, especially by employing specific angular increments [9–12]. The ability to capture the high temporal resolution images of the lungs allows for the characterization of dynamic respiratory processes, such as lung inflation and deflation, as well as the assessment of regional ventilation dynamics.

Radial UTE imaging techniques have emerged as a promising technique for enabling imaging of lung tissues with its intrinsically short $T_2^\star$ relaxation times [7, 13–15]. The application of radial UTE imaging in lung MRI not only enhances the visualization of lung structures but can also provide valuable information on tissue composition [16], lung density [17, 18], perfusion [2], and ventilation heterogeneity [1]. The combination of fast data acquisition and radial UTE imaging offers a comprehensive approach to evaluate lung function [15] and pathology [19–21], with improved accuracy and sensitivity.

However, in comparison to the Cartesian or radial encoding schemes [9], radial UTE sequences suffer from long acquisition times, due to the increased number of encodings required to fill the k-space. For more efficient encoding, the k-space sampling pattern can be improved by enhancing the coverage of the k-space for each interleave by using, e.g., a spiral trajectory [22, 23], but often disadvantageously increasing the read-out duration, which makes the sequence prone to off-resonance artifacts and $T_2^\star$-induced blur.

For more efficient sampling in combination with the advantageous sampling properties known from UTE, this work proposes a single-petal rosette trajectory [24, 25] (SPR), where the read-out and rephasing gradients used for radial UTE are replaced by a smooth gradient waveform, which intrinsically rephases to the k-space center, while non-redundantly encoding the k-space with only a negligible increase in TR. Furthermore, this sequence reduces the distinct stroke aliasing artifacts known from radial UTE and, due to starting each read-out in k_0, keeps the unique possibility of trading temporal vs. spatial resolution, inherent to radial UTE imaging. The suggested SPR sampling scheme also provides the possibility of reconstructing multiple images with different contrasts, due to the dual-echo sampling nature.

2 Methods

2.1 Trajectory design

Generally, one interleave (read-out) of the investigated SPR trajectories can be parameterized as

$$\begin{aligned}\mathbf{k}(t) &= k_x(t) + ik_y(t)\\ &= k_{\max}\sin(\omega t)e^{it},\end{aligned} \tag{1}$$

where ω accounts for the general shape of each rosette and is chosen from the interval $\omega \in \mathbb{R}$. For $t \in [0, \pi/\omega]$, the rosette reduces to a single petal, starting and ending in k_0.

The pre-factor $k_{\max}$ accounts for the extension of the k-space, i.e., which depends on the resolution since $k_{\max} = N/(2\mathrm{FOV})$, with N being the imaging matrix size in one dimension (isotropic) and FOV being the imaging field-of-view in one dimension (isotropic). Two parameterizations (ω = 5/3 and ω = 6/5) were chosen for further evaluation based on either the short read-out duration (ω = 5/3) or the advantageous k-space coverage (ω = 6/5), while keeping the read-out duration within an acceptable limit to reduce $T_2^\star$ blur. Further SPR trajectories were investigated in preliminary studies with the resulting acceptable scan parameters (as mentioned above), but no significant impact on image quality and functional values was observed.

The generated interleave is then rotated according to an angular increment of $\varphi_{n=7} = 23.6281^\circ$, corresponding to one specific tiny golden angle, enabling low-discrepancy sub-sampling properties for any number m of consecutively acquired interleaves as long as $m > 2n$ [26].

2.2 PSF analysis

Based on the SPR trajectory described in Section 2.1, the sampling point spread functions (PSFs) were derived for the trajectory parametrizations (ω = 5/3 and ω = 6/5). To obtain each PSF, unit k-space data were mapped onto a Cartesian grid [27, 28] and the calculated Voronoi tessellation was used to estimate the weights for compensating the sampling density of the non-uniformly acquired k-space data. The gridded data were then Fourier-transformed, yielding the PSF.

The side-lobe/peak ratio

$$\mathrm{SPR} = \max_{i\neq j}\left|\frac{\mathrm{PSF}(i,j)}{\mathrm{PSF}(i,i)}\right|, \tag{2}$$

of each PSF was further calculated to provide a measure for the coherence of the emerging aliasing artifacts [5].

For comparison, the same was repeated for the well-established radial UTE sampling scheme, as will be discussed in Section 2.3. For the simulation of the radial UTE PSF, the required densities were calculated analytically.

2.3 MR imaging and reconstruction

The images were acquired on a Philips 3T whole-body MRI (Ingenia 3.0T CX, Philips Healthcare, Best, Netherlands), using a 16ch dStream torso coil (Philips Healthcare, Best, Netherlands) in combination with an integrated 16ch posterior coil.

For this study, two SPR trajectories (ω = 5/3 and ω = 6/5) were calculated using MATLAB (MathWorks, Natick, Massachusetts, USA) and their respective gradient waveforms derived, ensuring the shortest read-out time under given gradient constraints (maximal gradient strength 20 mT/m and maximal slew rate 150 T/m/s). The $\mathrm{SPR}_{\omega=6/5}$ trajectory resulted in interleaves that are more circular in shape, i.e., the area enclosed by each rosette petal is increased as ω approaches 1. The trajectories are depicted in Figure 1. The read-out durations for $\mathrm{SPR}_{\omega=5/3}$ were $t_{\mathrm{acq},\,5/3}$ = 1.01 ms and $t_{\mathrm{acq},\,6/5}$ = 1.07 ms for the case $\mathrm{SPR}_{\omega=6/5}$.

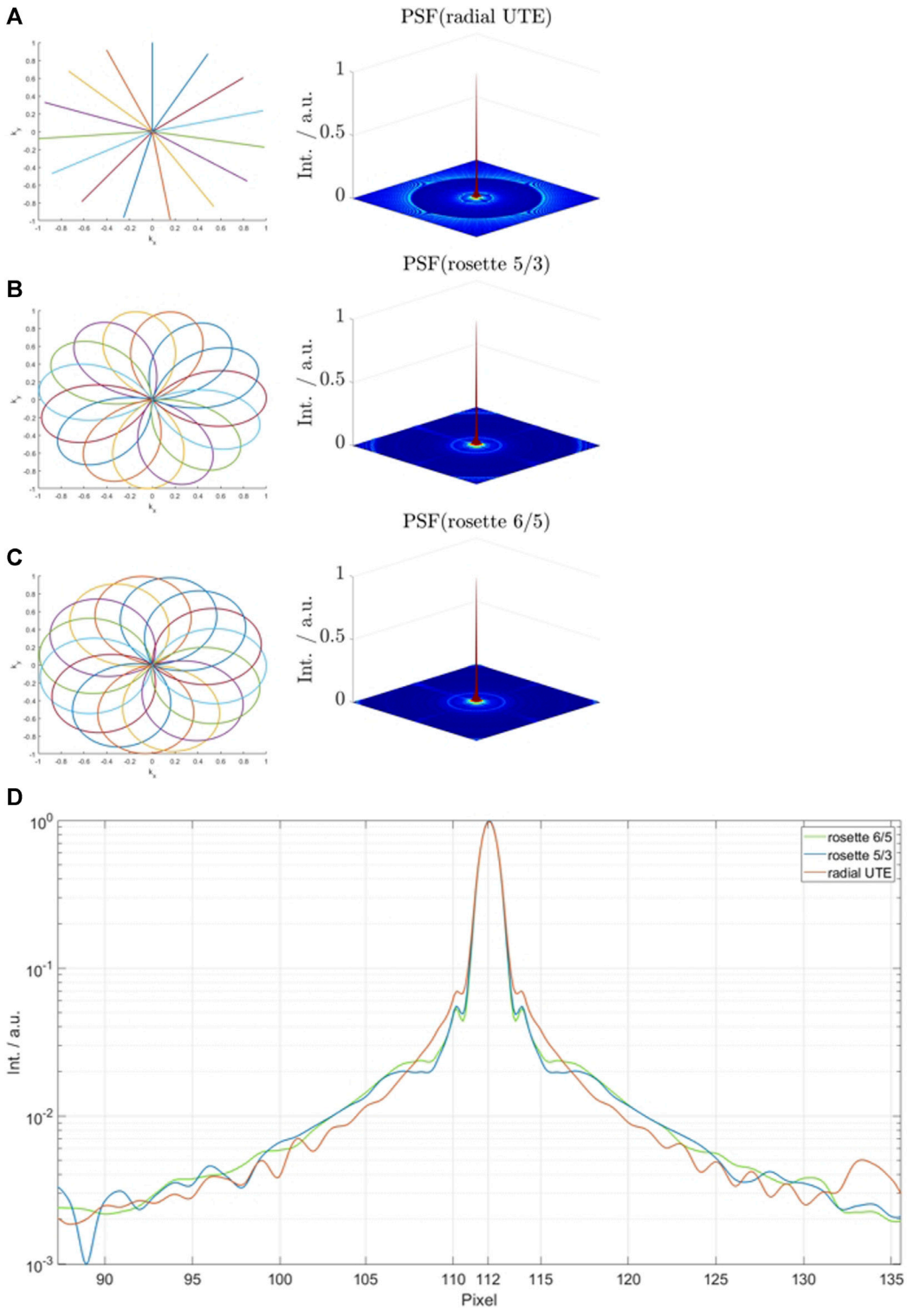

FIGURE 1
First 15 interleaves and simulated sampling point spread functions for radial ultra-short echo time (UTE) **(A)**, single-petal rosette trajectory ($SPR_{\omega=5/3}$) **(B)**, and $SPR_{\omega=6/5}$ **(C)**. **(D)** shows the spectral noise analysis for all trajectories.

After data acquisition, raw data were exported and processed with MATLAB (MathWorks, Natick, Massachusetts, USA). Images were obtained using gridding [29], with an oversampling factor of 1.25, a Kaiser–Bessel kernel for interpolation, and in combination with a 2D Voronoi tessellation for density compensation. During trajectory calculation, gradient delays were carefully considered [30] and remaining eddy current-induced distortions modeled by a mono-exponential decay function [31] with the time constant of

TABLE 1 Scan parameters for the 2D breath-hold SPR acquisitions and radial UTE acquisitions.

2D acquisition	$SPR_{\omega=5/3}$	$SPR_{\omega=6/5}$	Radial UTE
FOV/mm	450 × 450	450 × 450	450 × 450
Slice thickness/mm	20	20	20
Matrix	224 × 224	224 × 224	224 × 224
Res./mm	2 × 2 (in-plane)	2 × 2 (in-plane)	2 × 2 (in-plane)
TR/ms	3.1	3.2	2.6
TE/ms	0.45	0.45	0.45
No. of read-outs	703	703	703
Flip angle/°	6	6	6
Scan duration/s	2.39	2.44	1.99

τ = 43 μs. No post-processing was applied to any of the presented images.

In vivo imaging was performed in eight healthy volunteers with no reported respiratory disorders. Written informed consent was obtained prior to the examination. The imaging slice was centered at the bifurcation of the trachea in a coronal orientation.

Considering the SPR trajectory, the said slice was measured three times for each of the two trajectories ($SPR_{\omega=5/3}$ and $SPR_{\omega=6/5}$): once in the inhalation state (breath-hold); once in the exhalation state (breath-hold), each for a duration of 2.4 s; and once continuously during free breathing for a total scan duration of 113 s. For comparison, the same was repeated using radial UTE sampling with equal TE, whereas TR was kept minimal at 2.6 ms, resulting in a total scan duration of 1.99 s, in case of the breath-hold acquisitions, and 93 s in case of the free-breathing acquisition, for the same number of interleaves as for the SPR trajectories. In every case, the number of interleaves was equal to the number of interleaves required by the Nyquist sample k-space based on the radial UTE sampling scheme (703 interleaves), leading to oversampling in case of the SPR trajectories. All relevant scan parameters for the breath-hold acquisitions are shown in Table 1.

Due to the prolonged read-out duration in the SPR, $T_2^\star$ effects become more apparent, leading to changes in contrast in comparison to radial UTE sampling. To evaluate the capabilities of the proposed sampling scheme, SPR acquisitions were also retrospectively reconstructed based on only every first (center-out) or second (out-center) half of each SPR interleave.

Additionally, to take advantage of the oversampling of the SPR trajectory compared to the radial UTE, only the first 350 interleaves of every SPR acquisition were reconstructed for breath-hold images, reducing the total scan time to 1.28 s for $SPR_{\omega=5/3}$ and 1.31 s for $SPR_{\omega=6/5}$.

A sliding-window approach was used for the reconstruction of the real-time data. The increment was chosen as 100 ms with bin sizes of 703 read-outs, 300 read-outs, and 100 read-outs per frame for each investigated trajectory. Only the full-petal SPR trajectories were used for real-time and self-gating reconstruction.

Based on the free-breathing acquisitions, retrospective image-based self-gating was performed by deriving a respiratory navigator signal from images reconstructed with a high temporal resolution (100 ms) by manually identifying a line profile over the lung–liver interface (LLI) and, subsequently, obtaining the actual location of the LLI by gradient analysis. For determination of the respiratory stages, the data were binned based on equidistantly subdividing each stage based on the total displacement. For all further analyses of the gated images, the end-inspiratory and end-expiratory stages were chosen and compared to the breath-hold images.

2.4 Image analysis and functional parameters

For the assessment of regional ventilation in all images, the parenchyma was segmented semi-automatically by manually drawing approximate contours around the left and right lungs and by subsequently applying intensity thresholds to exclude large vessels.

According to [1], fractional ventilation values were calculated as follows:

$$FV = \frac{SI_{EX} - SI_{IN}}{SI_{EX}}, \tag{3}$$

with SI_{EX} and SI_{IN} being the pixel intensities in the images reconstructed for the expiration and inspiration breath-holds, respectively.

The signal-to-noise ratio (SNR) of the lung parenchyma was calculated according to [32] by

$$SNR = \sqrt{2 - \frac{\pi}{2}}\,\frac{SI_{ROI}}{\sigma_{BG}}, \tag{4}$$

where SI_{ROI} is the mean intensity within a selected ROI and σ_{BG} is the noise standard deviation of the pixel intensities within a selected background ROI. The square-root pre-factor corrects for the Rician distribution of noise in the evaluated magnitude images.

It has been shown that the breathing amplitude during breath-hold imaging impacts the FV reproducibility [33, 34] therefore, structural similarity (SSIM) analysis of the FV maps was performed, using the radial UTE-derived FV map as a reference.

The image sharpness assessment was carried out across an intensity line profile over the LLI. The position of the pixels corresponding to 25% and 75% of the maximum signal intensity was identified by a standard metric [35, 36], and the resulting distance was used as a sharpness measure.

To check for statistically significant differences in the SNR and FV, a paired two-sided Student's *t*-test was performed, with *p*-values smaller than 0.05 considered significant.

3 Results

3.1 PSF analysis

Figure 1 shows the normalized simulated sampling point spread functions for the investigated trajectories (A–C) and a logarithmic plot of the center regions of each PSF (D). The side-lobe/peak ratio is highest for the radial UTE trajectory ($69.7 \cdot 10^{-3}$). The side-lobe/peak ratio for the $SPR_{\omega=5/3}$ trajectory is reduced by 19.5% and reduced by 22.7% for $SPR_{\omega=6/5}$.

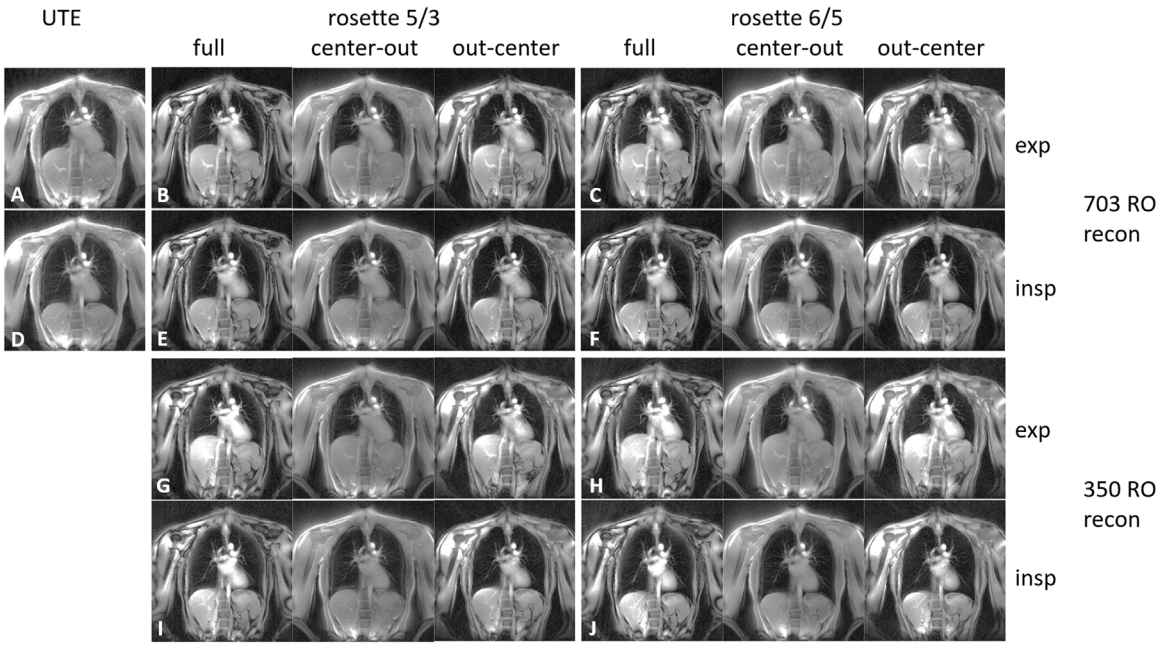

FIGURE 2
2D coronal lung images for expiration **(A–C** and **G–H)** and inspiration **(D–F** and **I–J)**. The images were acquired using radial UTE **(A, D)**, the $SPR_{\omega=5/3}$ trajectory **(B, E, G, and I)**, and the $SPR_{\omega=6/5}$ trajectory **(C, F, H, and J)**. The images corresponding to the SPR trajectories **(B, C, and E–J)** were reconstructed using the full petal, the first center-out half of the petal, and the second half of the petal. Images **(A–F)** were reconstructed using all 703 read-outs equaling a full Nyquist sampled *k*-space for radial UTE, whereas images **(G–J)** were reconstructed using only 350 read-outs.

3.2 Image quality and sharpness

Data acquisition was completed successfully for all volunteers. The breath-hold images of one volunteer are shown in Figure 2. The overall image quality is comparable for all reconstructed images. The fat-water shift-induced blur artifacts are visible in the low-signal parts of the radial UTE and the center-out SPR images, caused by non-fat-suppressed excitation. A markedly reduced fat signal can be observed in the full-petal SPR image, whereas the first half-petal SPR images show a radial UTE-like contrast. The out-center images lack the data of the first echo and, thus, show low signal left in the parenchyma.

The real-time reconstructed images can be found in the Supplementary Material S1–S9. The sharpness of the lung–liver interface increases for the lower number of read-outs per frame for all trajectories. The radial UTE images show the well-known aliasing artifacts in the form of distinct spokes, where in the SPR images, the aliasing results show less-pronounced, more noise-like artifacts.

The reconstructed breath-hold and gated images including the line profile across the LLI, used for sharpness analysis of one volunteer, are shown in Figure 3. The mean image sharpness for the self-gated images significantly increased for the end-expiratory stage, by 269.5% for $SPR_{\omega=5/3}$ (p <0.01) and 142.0% for $SPR_{\omega=6/5}$ (p <0.05), when compared to radial UTE. For the end-inspiratory stage images, sharpness increased when comparing $SPR_{\omega=5/3}$ to radial UTE, although insignificantly, by a mean of 53.9% (p <0.4), whereas for $SPR_{\omega=6/5}$ images, the sharpness decreased insignificantly by a mean of 25.5% (p <0.3).

No significant difference in image sharpness was found for breath-hold images when comparing radial UTE- and SPR-based images.

3.3 SNR

3.3.1 Breath-hold images

The mean SNR values in the lung parenchyma can be found in Table 2. The calculated SNR values were significantly higher for full-petal SPR compared to the radial UTE trajectory (p <0.01 for $SPR_{\omega=5/3}$ and p <0.02 for $SPR_{\omega=6/5}$) and for center-out read-outs (p <0.01 for $SPR_{\omega=5/3}$ and p <0.02 for $SPR_{\omega=6/5}$). The second half of the petal had significantly lower SNR values compared to the radial UTE (p <0.001 for $SPR_{\omega=5/3}$ and $SPR_{\omega=6/5}$). For the data that were reconstructed with the first 350 read-outs of the SPR trajectories, the SNR was significantly higher (p <0.05) when using the $SPR_{\omega=5/3}$ for both the full petal and the center-out half of the petal, compared to the full Nyquist-sampled radial UTE. The SNR was significantly higher (p <0.02) when using $SPR_{\omega=6/5}$ with only the first 350 read-outs for the center-out half of the petal, but no significant difference for the full petal compared to the full Nyquist-sampled radial UTE was found.

For both parametrizations of the SPR trajectory, the second half of the petal yielded a significantly lower (p <0.002) SNR compared to the full Nyquist-sampled radial UTE when only using the first 350 read-outs for reconstruction, as well as for reconstruction with all 703 read-out reconstructions.

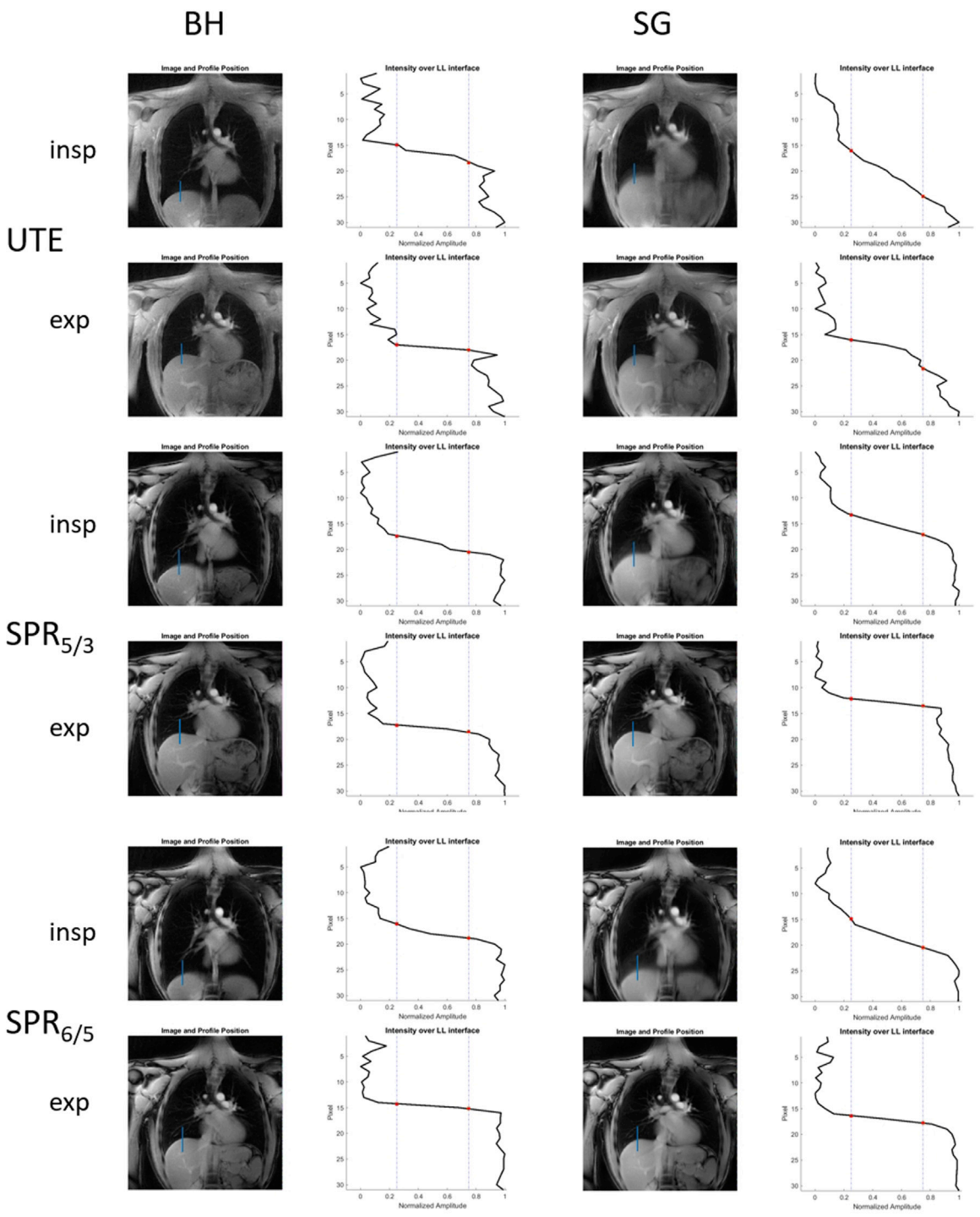

FIGURE 3
Reconstructed breath-hold and self-gated images acquired with radial UTE, $SPR_{\omega=5/3}$, and $SPR_{\omega=6/5}$, including corresponding line profiles across the LLI that are subsequently used for image sharpness analysis.

3.3.2 Self-gated images

The difference in the SNR values of the parenchyma between the self-gated, radial UTE-based images and the self-gated, SPR-based images was not significant for either trajectory (p <0.4 for $SPR_{\omega=5/3}$ during end-inspiration and p <0.2 for $SPR_{\omega=5/3}$ during end-expiration; p >0.5 for $SPR_{\omega=6/5}$ during end-inspiration and p >0.5 for $SPR_{\omega=6/5}$ during end-expiration).

10.3389/fphy.2024.1360083

TABLE 2 Mean SNR values in the lung parenchyma for the breath-hold images of all trajectories for 703 interleaves and for all reconstructions of SPR trajectories using only 350 interleaves.

		$SPR_{\omega=5/3}$			$SPR_{\omega=6/5}$		Radial UTE
703 interleaves	Full	Center-out	Out-center	Full	Center-out	Out-center	
Inspiration	5.0 ± 0.9	5.2 ± 0.4	2.5 ± 1.1	4.7 ± 0.8	5.4 ± 1.0	2.3 ± 0.8	4.4 ± 0.8
Expiration	5.9 ± 1.1	6.0 ± 0.8	2.9 ± 1.3	5.5 ± 1.0	6.0 ± 0.5	2.5 ± 0.9	4.7 ± 0.8
350 interleaves							
Inspiration	4.8 ± 0.5	4.9 ± 0.7	3.0 ± 1.2	4.4 ± 0.7	4.9 ± 0.5	2.7 ± 1.3	
Expiration	5.5 ± 0.7	5.2 ± 0.5	3.2 ± 1.2	5.0 ± 0.8	5.3 ± 0.5	3.0 ± 1.5	

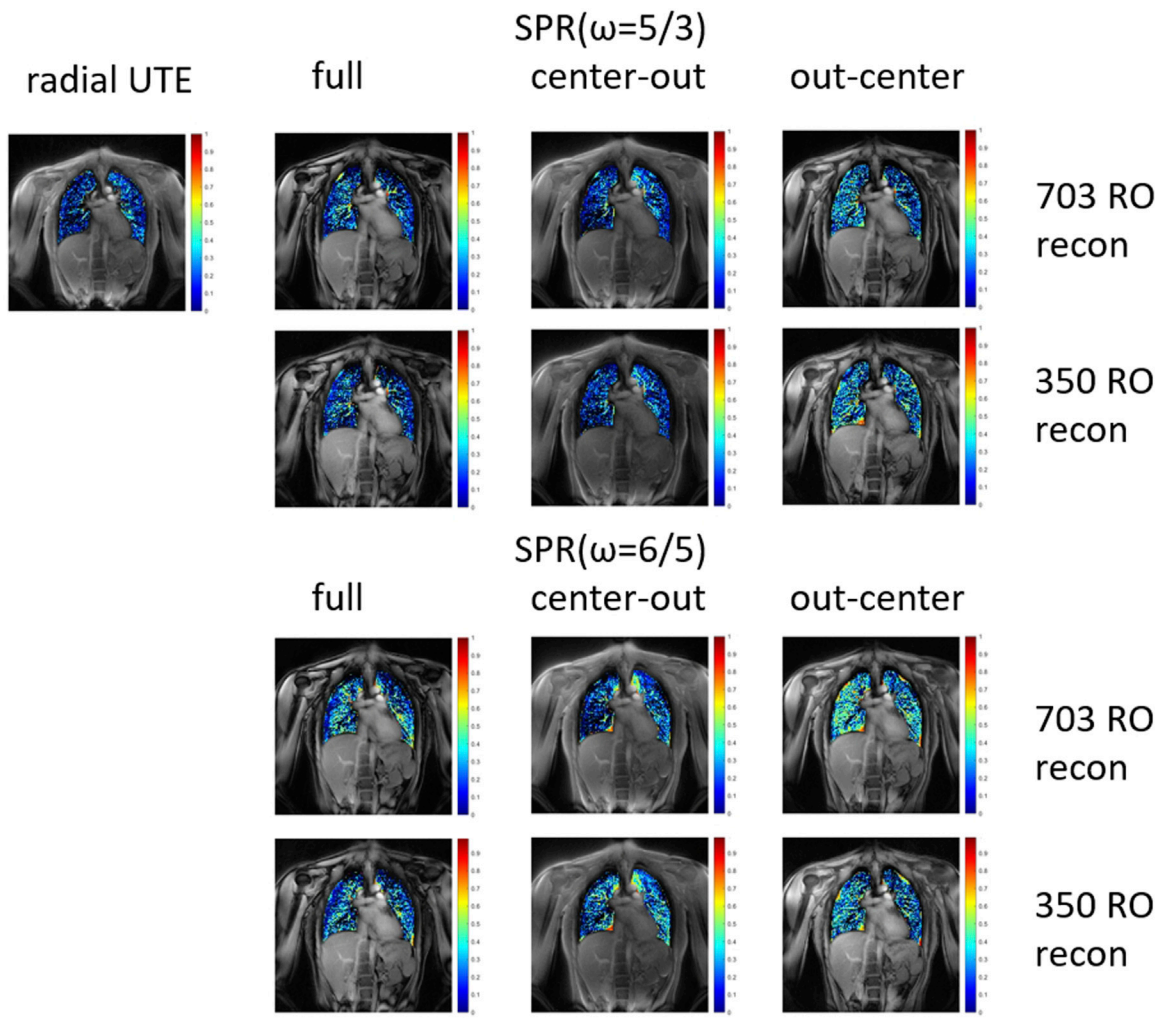

FIGURE 4
Fractional ventilation maps for radial UTE and both parametrizations of the SPR trajectory. The SPR trajectories were reconstructed for the full petal, first half of the petal, and second half of the petal. All trajectories were reconstructed using all 703 read-outs, corresponding to a fully Nyquist sampled *k*-space for radial UTE. Additionally, the SPR trajectories were reconstructed with only using the first 350 read-outs.

3.4 Functional values

3.4.1 Breath-hold images

The fractional ventilation maps are shown in Figure 4. No significant difference in fractional ventilation values was observed between the SPR trajectories and radial UTE. The mean fractional ventilation values are listed in Table 3. The SSIM index for the $SPR_{\omega=5/3}$ was calculated to be 0.81 for the full, first-half, and second-half petal and 0.82 for the full, first-half and second-half petal of $SPR_{\omega=6/5}$.

TABLE 3 Fractional ventilation values for breath-hold images of all trajectories and self-gated images. No significant differences between the SPR and radial UTE trajectories were found.

Breath-hold	$SPR_{\omega=5/3}$			$SPR_{\omega=6/5}$			Radial UTE
	Full	Center-out	Out-center	Full	Center-out	Out-center	
Mean FV	0.30	0.26	0.30	0.31	0.30	0.32	0.33
Self-gated	Full			Full			
Mean FV	0.23			0.25			0.21

3.4.2 Self-gated images

Similar to the breath-hold images, no significant difference in fractional ventilation values between the self-gated, radial UTE-based images and the self-gated, SPR-based images was found for either trajectory (p <0.2 for $SPR_{\omega=5/3}$ and p >0.5 for $SPR_{\omega=6/5}$).

4 Discussion

The general advantage of SPR trajectories is their intrinsic oversampling of the k-space compared to radial UTE sampling if an equal number of interleaves is considered. This is caused by the general petal shape of each interleave and the acquisition of non-redundant k-space data during rephasing (second half of each petal). Consequently, distinct advantages corresponding to relative k-space oversampling can be observed in the simulations of the sampling point spread functions as well as in significant increases in the SNR during, e.g., lung imaging.

The real-time reconstructions show notably better image quality for the high temporal resolution images acquired using the SPR trajectories, due to the more efficient k-space sampling pattern of the SPR trajectories compared to the radial UTE. The temporal resolution can be increased to even resolve the heart beat in case of the SPR trajectories, whereas the images acquired with radial UTE show more pronounced artifacts.

In separate reconstructions, images based on only the second half of each petal show a significant decrease in the SNR due to $T_2^\star$ relaxation, in comparison to images based on the first half of all petals. Nevertheless, for the presented application, the second half of each petal still introduces sufficient spatial frequency data above the noise floor to reduce aliasing artifacts from long T2 components and, as such, improved the image quality in the lungs.

The significantly higher SNR values of the SPR trajectories with a total number of interleaves that corresponds to Nyquist UTE sampling suggests that an undersampling factor of 2 might still be acceptable to obtain functional values that do not significantly deviate from the fully sampled case. This was especially true for $SPR_{\omega=5/3}$ acquisition, where a reconstruction with 350 instead of 703 interleaves still yielded a significantly higher SNR than that of Nyquist-sampled UTE imaging. Approximately equal SNR values were observed for $SPR_{\omega=6/5}$ (compared to radial UTE) where the decrease in the SNR relative to $SPR_{\omega=5/3}$ is most likely to be linked to the longer read-out durations, leading to more pronounced effects of $T_2^\star$ relaxation.

The low-fat signal in the full-petal images arises due to the dual sampling of k_0 acquisition of the SPR approach, where the second sampling of k_0 occurs at 1.01 ms for $SPR_{\omega=5/3}$ and at 1.07 ms for $SPR_{\omega=6/5}$, which is slightly below the point at which a 180° phase shift between fat and water is established (1.1 ms for 3T). This property of intrinsic fat suppression might be advantageous regarding image blur and aliasing artifact introduced from a high-signal fat component. With the currently chosen read-out duration in the order of 1 ms, the sampling of the k-space center during the second echo yields a marked reduction in the fat signal, resulting in the reduction of high-intensity aliasing artifacts. Furthermore, the high-intensity aliasing artifacts are less pronounced in the out-center SPR images since a phase cancellation similar to intravoxel dephasing in pixel containing both water and fat occurs.

The analysis of FV maps resulted in no significant difference in the FV values between radial UTE and the proposed SPR trajectories. Additionally, the structural similarity of the FV maps suggests that the SPR trajectories present a viable alternative to radial UTE concerning functional analysis of lung data.

Retrospective image-based self-gating yielded comparable or higher SNR values when performed for SPR-based images compared to radial UTE-based images. Image sharpness increased significantly for the end-expiratory stage for SPR-based images compared to radial UTE-based images, whereas no significant difference was found for the end-inspiratory stage. Fractional ventilation values also yielded no significant difference.

From a clinical perspective, the full, isotropic 3D coverage of the lungs appears beneficial. In principle, the application of 3D techniques like ZTE or 3D variants of UTE including 3D radial UTE and 3D rosettes has been shown to be capable of providing anatomic and functional data of the lungs. However, the related long scan times limit the application of the 3D approaches, which are often not well-tolerated by the patients suffering from lung disease. In that respect, the rapid subsequent acquisition of 2D slices renders an attractive and maybe clinically more usable alternative. Here, the suggested single-petal approach may especially be beneficial due to its superior SNR performance, which can be applied to either improve the image quality or speed up data acquisition. Furthermore, the dual measurement of k_0 can be used for contrast manipulations and especially for reduction of the fat signal. This holds potential for further reduction of aliasing artifacts from high-signal (fat) components overlaid onto the low-signal lungs and may enable to further improve the temporal resolution in the real-time acquisitions.

5 Conclusion

The oversampling properties of the proposed SPR trajectory lead to significant improvements in the SNR compared to radial UTE sampling by accepting only minimal increases in TR. Furthermore, the SPR trajectories outperform radial UTE sampling, even with less

than half the number of read-outs in terms of the SNR. This can be used to decrease scan times, which is especially useful for breath-hold imaging, to enhance the temporal resolution in real-time imaging and for gating approaches where the temporal resolution is of great importance.

Fractional ventilation values of the proposed SPR trajectories, which are compared to those obtained from images acquired using a radial UTE trajectory, suggest that the proposed trajectories are suitable for functional lung imaging.

As a further advantage, multiple contrasts can be reconstructed from data acquired with the SPR sequence, including radial UTE-like contrast, by only using the first half of the petal and a low-fat contrast by exploiting the position of the second echo of the SPR trajectory.

The SPR trajectories have proven feasible for retrospective image-based self-gating, thus making SPR trajectories an excellent candidate for further investigations in lung MRI. An extension to 3D imaging could be considered to profit from shorter echo times due to the lack of slice selection. Their comparison to other trajectories, such as the ZTE, needs to be considered.

Data availability statement

The original contributions presented in the study are included in the article/Supplementary Material; further inquiries can be directed to the corresponding author.

Ethics statement

The studies involving humans were approved by Ethikkommission der Universität Ulm. The studies were conducted in accordance with the local legislation and institutional requirements. The participants provided their written informed consent to participate in this study.

Author contributions

HF: conceptualization, data curation, formal analysis, investigation, methodology, software, validation, visualization, writing–original draft, and writing–review and editing. TS: writing–original draft and writing–review and editing. VR: conceptualization, funding acquisition, supervision, and writing–review and editing.

Funding

The author(s) declare that financial support was received for the research, authorship, and/or publication of this article. This work was funded by the German Research Foundation under grant agreement 465599659.

Acknowledgments

The authors thank the Ulm University Centre for Translational Imaging MoMAN for its support. The continuous support by Philips Healthcare is highly appreciated by the authors.

Conflict of interest

The authors declare that the research was conducted in the absence of any commercial or financial relationships that could be construed as a potential conflict of interest.

Publisher's note

All claims expressed in this article are solely those of the authors and do not necessarily represent those of their affiliated organizations, or those of the publisher, the editors, and the reviewers. Any product that may be evaluated in this article, or claim that may be made by its manufacturer, is not guaranteed or endorsed by the publisher.

Supplementary material

The Supplementary Material for this article can be found online at: https://www.frontiersin.org/articles/10.3389/fphy.2024.1360083/full#supplementary-material

References

1. Zapke M, Topf H, Mea Z, Kuth R, Deimling M, Kreisler P, et al. Magnetic resonance lung function – a breakthrough for lung imaging and functional assessment? a phantom study and clinical trial. *Respir Res* (2006) 7:106. doi:10.1186/1465-9921-7-106

2. Wielpütz M, Kauczor HU. Mri of the lung: state of the art. *Diagn Interv Radiol* (2012) 18:344–53. doi:10.4261/1305-3825.dir.5365-11.0

3. Pruessmann KP, Weiger M, Scheidegger MB, Boesiger P. Sense: sensitivity encoding for fast mri. *Magn Reson Med Official J Int Soc Magn Reson Med* (1999) 42:952–62. doi:10.1002/(sici)1522-2594(199911)42:5<952::aid-mrm16>3.3.co;2-j

4. Griswold MA, Blaimer M, Breuer F, Heidemann RM, Mueller M, Jakob PM. Parallel magnetic resonance imaging using the grappa operator formalism. *Magn Reson Med* (2005) 54:1553–6. doi:10.1002/mrm.20722

5. Lustig M, Donoho D, Pauly JM. Sparse MRI: the application of compressed sensing for rapid MR imaging. *Magn Reson Med* (2007) 58(6):1182–95. doi:10.1002/mrm.21391

6. Lustig M, Donoho DL, Santos JM, Pauly JM. Compressed sensing mri. *IEEE Signal Processing Magazine* (2008) 25:72–82. doi:10.1109/msp.2007.914728

7. Bergin CJ, Pauly JM, Macovski A. Lung parenchyma: projection reconstruction mr imaging. *Radiology* (1991) 179:777–81. doi:10.1148/radiology.179.3.2027991

8. Weiger M, Brunner DO, Dietrich BE, Müller CF, Pruessmann KP. Zte imaging in humans. *Magn Reson Med* (2013) 70:328–32. doi:10.1002/mrm.24816

9. Wild JM, Marshall H, Bock M, Schad LR, Jakob PM, Puderbach M, et al. Mri of the lung (1/3): methods. *Insights into imaging* (2012) 3:345–53. doi:10.1007/s13244-012-0176-x

10. Biederer J, Beer M, Hirsch W, Wild J, Fabel M, Puderbach M, et al. Mri of the lung (2/3). why. when how? *Insights into imaging* (2012) 3:355–71. doi:10.1007/s13244-011-0146-8

11. Hatabu H, Alsop DC, Listerud J, Bonnet M, Gefter WB. T2* and proton density measurement of normal human lung parenchyma using submillisecond echo time gradient echo magnetic resonance imaging. *Eur J Radiol* (1999) 29:245–52. doi:10.1016/s0720-048x(98)00169-7

12. Bae K, Jeon KN, Hwang MJ, Lee JS, Ha JY, Ryu KH, et al. Comparison of lung imaging using three-dimensional ultrashort echo time and zero echo time sequences: preliminary study. *Eur Radiol* (2019) 29:2253–62. doi:10.1007/s00330-018-5889-x

13. Yu J, Xue Y, Song HK. Comparison of lung t2* during free-breathing at 1.5 t and 3.0 t with ultrashort echo time imaging. *Magn Reson Med* (2011) 66:248–54. doi:10.1002/mrm.22829

14. Johnson KM, Fain SB, Schiebler ML, Nagle S. Optimized 3d ultrashort echo time pulmonary mri. *Magn Reson Med* (2013) 70:1241–50. doi:10.1002/mrm.24570

15. Balasch A, Metze P, Stumpf K, Beer M, Büttner SM, Rottbauer W, et al. 2d ultrashort echo-time functional lung imaging. *J Magn Reson Imaging* (2020) 52:1637–44. doi:10.1002/jmri.27269

16. Torres L, Kammerman J, Hahn AD, Zha W, Nagle SK, Johnson K, et al. Structure-function imaging of lung disease using ultrashort echo time mri. *Acad Radiol* (2019) 26:431–41. doi:10.1016/j.acra.2018.12.007

17. Togao O, Tsuji R, Ohno Y, Dimitrov I, Takahashi M. Ultrashort echo time (ute) mri of the lung: assessment of tissue density in the lung parenchyma. *Magn Reson Med* (2010) 64:1491–8. doi:10.1002/mrm.22521

18. Higano NS, Fleck RJ, Spielberg DR, Walkup LL, Hahn AD, Thomen RP, et al. Quantification of neonatal lung parenchymal density via ultrashort echo time mri with comparison to ct. *J Magn Reson Imaging* (2017) 46:992–1000. doi:10.1002/jmri.25643

19. Ma W, Sheikh K, Svenningsen S, Pike D, Guo F, Etemad-Rezai R, et al. Ultra-short echo-time pulmonary mri: evaluation and reproducibility in copd subjects with and without bronchiectasis. *J Magn Reson Imaging* (2015) 41:1465–74. doi:10.1002/jmri.24680

20. Veldhoen S, Weng AM, Knapp J, Kunz AS, Stäb D, Wirth C, et al. Self-gated non–contrast-enhanced functional lung mr imaging for quantitative ventilation assessment in patients with cystic fibrosis. *Radiology* (2017) 283:242–51. doi:10.1148/radiol.2016160355

21. Woods JC, Wild JM, Wielpütz MO, Clancy JP, Hatabu H, Kauczor HU, et al. Current state of the art mri for the longitudinal assessment of cystic fibrosis. *J Magn Reson Imaging* (2020) 52:1306–20. doi:10.1002/jmri.27030

22. Cha MJ, Park HJ, Paek MY, Stemmer A, Lee ES, Park SB, et al. Free-breathing ultrashort echo time lung magnetic resonance imaging using stack-of-spirals acquisition: a feasibility study in oncology patients. *Magn Reson Imaging* (2018) 51:137–43. doi:10.1016/j.mri.2018.05.002

23. Huang YS, Niisato E, Su MYM, Benkert T, Hsu HH, Shih JY, et al. Detecting small pulmonary nodules with spiral ultrashort echo time sequences in 1.5 t mri. *Magn Reson Mater Phys Biol Med* (2021) 34:399–409. doi:10.1007/s10334-020-00885-x

24. Noll DC. Multishot rosette trajectories for spectrally selective mr imaging. *IEEE Trans Med Imaging* (1997) 16:372–7. doi:10.1109/42.611345

25. Noll DC, Peltier SJ, Boada FE. Simultaneous multislice acquisition using rosette trajectories (smart): a new imaging method for functional mri. *Magn Reson Med* (1998) 39:709–16. doi:10.1002/mrm.1910390507

26. Wundrak S, Paul J, Ulrici J, Hell E, Geibel MA, Bernhardt P, et al. Golden ratio sparse mri using tiny golden angles. *Magn Reson Med* (2016) 75:2372–8. doi:10.1002/mrm.25831

27. Rasche V, Proksa R, Sinkus R, Bornert P, Eggers H. Resampling of data between arbitrary grids using convolution interpolation. *IEEE Trans Med Imag* (1999) 18:385–92. doi:10.1109/42.774166

28. Speidel T, Metze P, Rasche V. Efficient 3D low-discrepancy *k*-space sampling using highly adaptable seiffert spirals. *IEEE Trans Med Imaging* (2019) 38:1833–40. doi:10.1109/TMI.2018.2888695

29. Beatty PJ, Nishimura DG, Pauly JM. Rapid gridding reconstruction with a minimal oversampling ratio. *IEEE Trans Med Imaging* (2005) 24:799–808. doi:10.1109/tmi.2005.848376

30. Robison RK, Devaraj A, Pipe JG. Fast, simple gradient delay estimation for spiral mri. *Magn Reson Med* (2010) 63:1683–90. doi:10.1002/mrm.22327

31. Atkinson IC, Lu A, Thulborn KR. Characterization and correction of system delays and eddy currents for mr imaging with ultrashort echo-time and time-varying gradients. *Magn Reson Med* (2009) 62:532–7. doi:10.1002/mrm.22016

32. Constantinides CD, Atalar E, McVeigh ER. Signal-to-noise measurements in magnitude images from nmr phased arrays. *Magn Reson Med* (1997) 38:852–7. doi:10.1002/mrm.1910380524

33. Klimeš F, Voskrebenzev A, Gutberlet M, Kern A, Behrendt L, Kaireit T, et al. Free-breathing quantification of regional ventilation derived by phase-resolved functional lung (preful) mri. *NMR Biomed* (2019) 32:e4088. doi:10.1002/nbm.4088

34. Yang B, Metze P, Balasch A, Stumpf K, Beer M, Rottbauer W, et al. Reproducibility of functional lung parameters derived from free-breathing non-contrast-enhanced 2d ultrashort echo-time. *Quantitative Imaging Med Surg* (2022) 12:4720–33. doi:10.21037/qims-22-92

35. Larson AC, Kellman P, Arai A, Hirsch GA, McVeigh E, Li D, et al. Preliminary investigation of respiratory self-gating for free-breathing segmented cine mri. *Magn Reson Med Official J Int Soc Magn Reson Med* (2005) 53:159–68. doi:10.1002/mrm.20331

36. Wundrak S, Paul J, Ulrici J, Hell E, Geibel MA, Bernhardt P, et al. A self-gating method for time-resolved imaging of nonuniform motion. *Magn Reson Med* (2016) 76:919–25. doi:10.1002/mrm.26000